nature nanotechnology

LETTERS

https://doi.org/10.1038/s41565-018-0275-z

Deterministic coupling of site-controlled quantum emitters in monolayer WSe_2 to plasmonic nanocavities

Yue Luo[1,2], Gabriella D. Shepard[1,2], Jenny V. Ardelean[3], Daniel A. Rhodes[3], Bumho Kim[3], Katayun Barmak[3], James C. Hone[3] and Stefan Strauf[1,2]*

Solid-state single-quantum emitters are crucial resources for on-chip photonic quantum technologies and require efficient cavity–emitter coupling to realize quantum networks beyond the single-node level[1,2]. Monolayer WSe_2, a transition metal dichalcogenide semiconductor, can host randomly located quantum emitters[3–6], while nanobubbles[7] as well as lithographically defined arrays of pillars in contact with the transition metal dichalcogenide act as spatially controlled stressors[8,9]. The induced strain can then create excitons at defined locations. This ability to create zero-dimensional (0D) excitons anywhere within a 2D material is promising for the development of scalable quantum technologies, but so far lacks mature cavity integration and suffers from low emitter quantum yields. Here we demonstrate a deterministic approach to achieve Purcell enhancement at lithographically defined locations using the sharp corners of a metal nanocube for both electric field enhancement and to deform a 2D material. This nanoplasmonic platform allows the study of the same quantum emitter before and after coupling. For a 3 × 4 array of quantum emitters we show Purcell factors of up to 551 (average of 181), single-photon emission rates of up to 42 MHz and a narrow exciton linewidth as low as 55 μeV. Furthermore, the use of flux-grown WSe_2 increases the 0D exciton lifetimes to up to 14 ns and the cavity-enhanced quantum yields from an initial value of 1% to up to 65% (average 44%).

Although a number of approaches have been demonstrated for the deterministic cavity coupling of quantum dots[1,2,10–12] as well as nitrogen[13] and silicon[14] vacancy centres in diamond, scalability has been impeded because these approaches lack spatial control of quantum emitters, which form naturally only in random locations. One way considered to overcome this is site-controlled growth of quantum dots coupled to dielectric cavities, but the Purcell enhancement remained rather low, with a Purcell factor F_P of 4 (refs [15,16]). Appealing alternatives to dielectric cavities include nanoplasmonic gap mode resonators located in close proximity to quantum emitters, which are known to strongly enhance the light–matter interaction[17–19] as well as the quantum yield[20,21]. Most demonstrations rely on dispersing colloidal plasmonic nanocubes randomly onto a substrate containing emitters, and thus lack spatial control of the plasmonic hot spot with respect to the quantum emitter location[17,22,23]. With transition metal dichalcogenide (TMDC) integration, plasmonic silver islands were utilized to create quantum emitters in WSe_2, but this approach also lacked spatial control and displayed no pronounced coupling[24]. While DNA origami provides ultrahigh degrees of spatial control with 1 nm accuracy[25], the bottom-up approach has not been demonstrated to be scalable, and integration with TMDCs is not straightforward. In contrast, top-down fabrication can enable control of plasmonic hot spots on a wafer[20]. In this way, coupling of the plasmonic array mode was shown for boron nitride quantum emitters, but spatial control of the quantum emitter itself was lacking, and only a modest twofold Purcell enhancement was demonstrated because the gap mode was not utilized[26]. Deterministic coupling providing spatial control for both the quantum emitter and plasmonic gap mode in a scalable on-chip platform has thus remained an unsolved challenge.

In the experiment presented here, auto-coupling is accomplished by using the nanocube corners that form vertical plasmonic gap modes against a planar Au mirror (Fig. 1a), theoretically giving rise to a 900-fold intensity enhancement (Fig. 1b and Supplementary Note 1). The gap size itself is solely defined by layer deposition rather than lithography. The WSe_2 monolayer is surrounded by 2-nm-thick Al_2O_3 spacer layers on each side, resulting in a total gap size of 5 nm (Fig. 1a, inset). This spacer prevents optical quenching and spectral diffusion in the exciton emission[20]. Figure1c shows that hot spots are located at the four nanocube corners. Their spatial locations coincide with the occurrence of high strain areas in the stamped monolayer (Fig. 1d and Supplementary Note 2). The best results were found with a near-unity aspect ratio of flat-top cubes with a height of 90 nm and side length of 110 nm. Figure 1e shows a scanning electron microscope (SEM) image of a Au nanocube array with 2.5 μm pitch (see Methods). The small size of the nanocubes allows efficient extraction of the nanogap emission into the far field[17], while the transparent sapphire wafer allows the probing of quantum emitters even when the cavity is closed. The broadband response of the plasmonic mode (quality factor Q of ~8) was tailored to coincide with the exciton emission wavelength (750–800 nm), as depicted in Fig. 1f.

To characterize the success rate of quantum emitter formation, monolayer WSe_2 was stamped onto the nanocube array, but the planar Au layer depicted in Fig. 1a was not attached, thus comprising the 'uncoupled' case. As anticipated, the bright photoluminescence emission spots in Fig. 2a follow the lithographically defined locations in 57 of 60 cases, resulting in a success rate of 95% to find at least one quantum emitter per site. The SEM images in Fig. 2b verify that the material has been successfully transferred onto the nanocubes without being pierced. Spectra recorded from the nanocube locations show that quantum emission occurs within a well-defined wavelength range of 35 nm (755–790 nm), as highlighted by

[1]Department of Physics, Stevens Institute of Technology, Hoboken, NJ, USA. [2]Center for Quantum Science and Engineering, Stevens Institute of Technology, Hoboken, NJ, USA. [3]Department of Mechanical Engineering, Columbia University, New York, NY, USA. *e-mail: strauf@stevens.edu

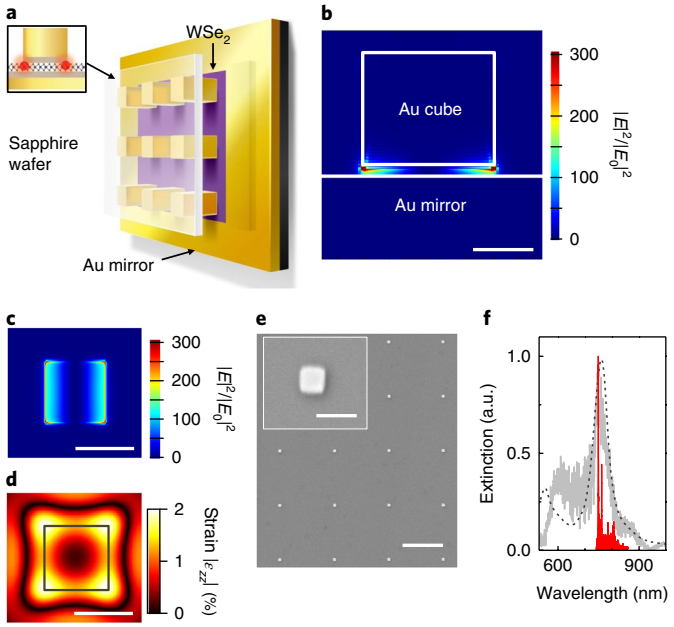

Fig. 1 | Overview of sample design enabling deterministic coupling of strain-induced excitons to nanoplasmonic gap modes. a, Schematic of monolayer WSe_2 coupled to a plasmonic Au nanocube cavity array. The WSe_2 is separated from the plasmonic Au cubes and the planar Au layer by a 2 nm Al_2O_3 spacer layer on each side to prevent optical quenching and short-circuiting of the nanoplasmonic gap mode (depicted by grey shading in the inset). The transparent sapphire wafer allows optical addressing of the quantum emitters. **b**, Side view of the simulated intensity enhancement ($|E|^2/|E_0|^2$) distribution profile illustrating confinement of the plasmon across the vertical gap containing the WSe_2. Scale bar, 50 nm. **c**, Top view of simulated $|E|^2/|E_0|^2$ showing four plasmonic hot spots at cube corners. Scale bar, 100 nm. **d**, Simulation of the strain profile induced in the WSe_2 layer when stamped onto a nanocube, showing that the highest strain occurs at cube corners coinciding with plasmonic hot spots. Scale bar, 100 nm. **e**, SEM image of the Au nanocube array on a sapphire substrate. Scale bar, 2 µm. Inset, Magnified view of an individual Au nanocube. Scale bar, 200 nm. **f**, Simulated (dashed line) and measured (grey solid line) plasmon resonance spectra together with the localized exciton spectrum (red solid line) of a typical quantum emitter directly induced by the Au nanocube into WSe_2, illustrating spectral resonance matching.

the shading in Fig. 2c. In most cases exactly four spectrally isolated emitters are found per site (Fig. 2d), with a mean value of 4.1 emitters per site (Fig. 2e), following precisely the expectation that each corner of a nanocube induces one quantum emitter with a high success rate (67%). We consider each observed spectrally sharp peak to be a single quantum emitter, with one example of pronounced single-photon antibunching in Fig. 2f that is characterized by a zero delay time value of $g^{(2)}(0) = 0.16 \pm 0.03$ (Supplementary Note 3). The statistical distribution in Fig. 2g shows $g^{(2)}(0)$ values well below 0.5 (grey dashed line) (average $g^{(2)}(0) = 0.22$), for 15 spectrally sharp lines selected from the array. It is also possible to resolve quantum light emission from all four quantum emitters on a specific nanocube site, as shown in Supplementary Note 4. As a result, quantum emitter formation via plasmonic nanocubes is spatially deterministic and occurs in a well-defined wavelength range (35 nm), which simplifies emitter–mode coupling. We have observed comparable results when transferring monolayer $MoSe_2$ onto the nanocube arrays, albeit with a larger ensemble background in the spectral vicinity of the induced sharp emission lines (Supplementary Note 5).

Emitter–mode coupling in plasmonic nanocavities has often been quantified by statistical averages comparing coupled emitters with another set of emitters located in reference samples[17,20]. Our sample design offers the unique ability to directly compare the optical properties of the same quantum emitter in its coupled and uncoupled state. To this end we devised the measurement scheme depicted in Fig. 3a,b, which first characterizes strain-induced excitons in the presence of the Au nanocubes, but without the planar Au mirror, such that the vertical gap mode is not established. The sample is then inverted and attached in contact with a planar Au mirror to characterize the coupled state. We note that forming the cavity leaves all quantum emitters intact, and the success rate of 95% for creating at least one quantum emitter is unchanged, with an average number of 4.2 quantum emitters per nanocube (Supplementary Note 6). Hyperspectral photoluminescence maps of an exemplary 3×4 quantum emitter array from the sample shown in Fig. 2 were recorded before (Fig. 3c, top) and after (Fig. 3c, bottom) introducing the Au mirror, and show that the quantum emitters are significantly brighter under coupling. To determine the light enhancement factor, the time-integrated intensity of an individual emitter was recorded as a function of excitation power under continuous-wave laser excitation (Fig. 3d). In the saturation region, the enhancement factor is 13, which is predominantly caused by an enhanced spontaneous emission rate (that is, an underlying Purcell effect), while enhanced absorption and light collection play a minor role (Supplementary Note 1).

To directly measure the spontaneous emission rate enhancement for an individual quantum emitter on the 3×4 array, we determined the total rate enhancement factor γ_{on}/γ_{off} via time-correlated single-photon counting (TCSPC), where γ_{on} and γ_{off} are the rates for the coupled and uncoupled case, respectively. Figure 3e shows the TCSPC traces for an exemplary quantum emitter with mono-exponential decay times of $\tau_{off} = 5{,}510 \pm 45$ ps and $\tau_{on} = 98 \pm 3$ ps. The shorter decay time yields a rate enhancement of $\gamma_{on}/\gamma_{off} = 57$. To show universal coupling we carried out TCSPC experiments tracking 12 quantum emitters and found an average lifetime $\tau_{off,av} = 4.0 \pm 1.8$ ns for the uncoupled case and $\tau_{on,av} = 266 \pm 120$ ps for the coupled case (Fig. 3f). As anticipated in the design, each strain-induced quantum emitter features a strong Purcell effect with an average γ_{on}/γ_{off} of 15, implying a 100% success rate of coupling within the selected range.

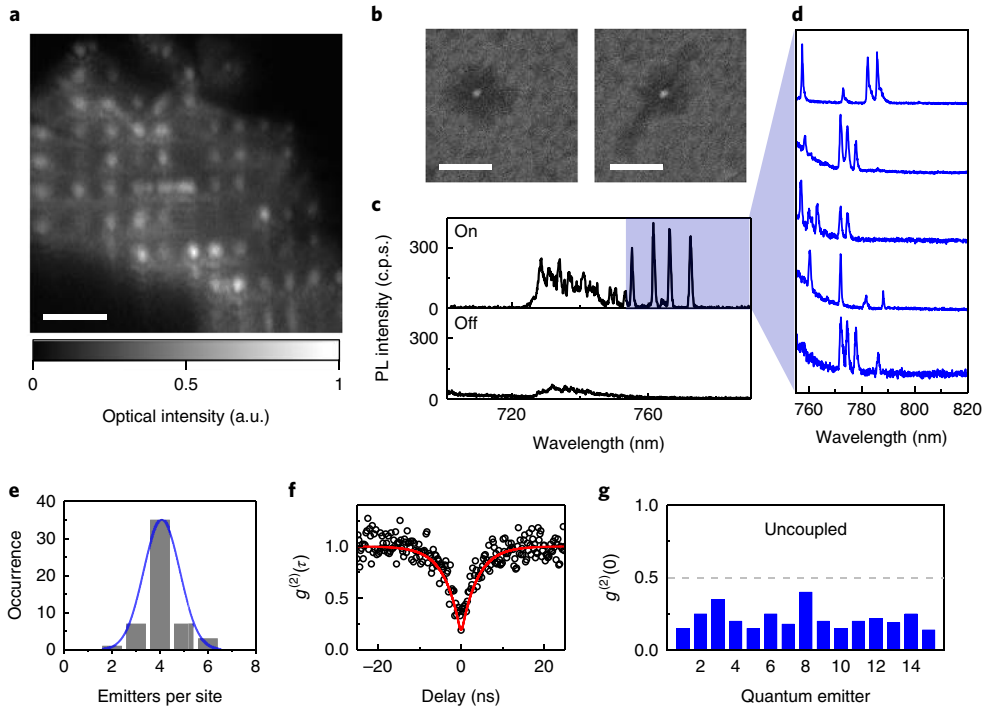

Fig. 2 | Optical characterization of strain-induced quantum emitters created by the nanocube array. a, Hyperspectral photoluminescence map of WSe_2 strained over a Au nanocube array filtered within the spectral range 750–850 nm, covering all localized exciton emission. Scale bar, 5 µm. **b**, SEM images of two selected locations, showing that the strained WSe_2 material remains elevated and undamaged for about 100–200 nm around the pillar location (darker electron signal at in-lens detector) before touching the substrate (brighter electron signal). Scale bars, 400 nm. **c**, Comparison of photoluminescence (PL) spectra when WSe_2 is strained over the Au nanopillars (top) and when WSe_2 rests on the substrate (bottom). c.p.s., counts per second. **d**, Example normalized photoluminescence spectra of isolated quantum emitters at Au pillar locations. **e**, Histogram of quantum emitter occurrence on the array, demonstrating the high success rate for creating four isolated quantum emitters per nanocube location. **f**, Second-order photon correlation function $g^{(2)}(\tau)$ recorded with a Hanbury Brown–Twiss type set-up under non-resonant excitation, which displays pronounced single-photon antibunching (black circles). The red solid line is a fit to the rate-equation analysis for an individual two-level system, resulting in a single-photon purity of $g^{(2)}(0) = 0.16 \pm 0.03$ and exciton recovery time of $\tau = 3.8 \pm 0.2$ ns. **g**, Single-photon purity values at zero delay time recorded for 15 quantum emitters on the array (before coupling).

The measured rate enhancement corresponds to the Purcell factor F_P only in the case of an emitter with unity quantum yield ($\eta = 100\%$). For imperfect quantum emitters with low quantum yield that are dominated by non-radiative recombination, the underlying F_P is much larger than the measured rate enhancement[20]. To determine F_P for our case we directly measured the quantum yield under pulsed excitation in the saturation regime, resulting in $\eta_{off} = 1.5 \pm 0.4\%$ for the uncoupled case and a Purcell-enhanced quantum yield of $\eta_{on} = 12.6 \pm 2\%$ (Supplementary Note 7). As is well known[20], the underlying F_P can in this case be calculated from the product of the measured rate enhancement $\gamma_{on}/\gamma_{off} = 57$ and the measured quantum yield enhancement $\eta_{on}/\eta_{off} = 13$, resulting in $F_P = 551$ for the best case (average $F_P = 181$) in Fig. 3f (Supplementary Note 8). Such a high F_P implies that the spontaneous emission coupling factor $\beta = F_P/(1 + F_P)$ is unity (99.9%); that is, the entire spontaneous emission is coupled to the nanogap mode. We confirmed that the single-photon purity was not compromised—one example, shown in Fig. 3g, yields $g^{(2)}(0) = 0.15 \pm 0.03$. Figure 3h shows the statistical distribution of 15 coupled quantum emitters displaying an average $g^{(2)}(0) = 0.21$ that matches the uncoupled case in Fig. 2g. Note that the Purcell-enhanced short lifetimes require pulsed excitation to overcome the detector jitter limit when recording $g^{(2)}(\tau)$ (Supplementary Note 3). The demonstrated on-demand generation of triggered single-photon emission onto clock states is also the technologically relevant case required for quantum information processing[27]. Taking the detection efficiency into account, the single-photon emission rate into the first lens reaches up to 10.6 MHz (Supplementary Note 7) under pulsed excitation (78 MHz repetition rate). As a result of deterministic emitter–mode coupling in our scheme, the quantum emitters display an average Purcell enhancement of single photons of two orders of magnitude, and a quantum yield enhancement of one order of magnitude.

With the goal of further enhancing the maximum achievable quantum yield for triggered single-photon emission, we explored two approaches to reduce the non-radiative recombination rate from WSe_2. The first approach utilizes magnetic brightening to convert dark excitons into bright excitons[28]. At 9 T, the strain-induced quantum emitters display a 35% optical brightening as well as a 36% faster decay rate of $\tau_{on,B} = 72$ ps for the coupled cased (Supplementary Note 9). As a result, the quantum yield for the coupled emitter increases from 12.6% at zero field to 14.9% at 9 T. The second approach directly reduces non-radiative recombination centres by controlling the defect density during material growth. The often-utilized chemical vapour transport (CVT) growth of WSe_2 suffers from high point defect densities, typically above 1×10^{12} cm^{-2}. In contrast, our flux growth technique (see Methods) achieves a reduction in defect density of more than one order of magnitude, typically 7×10^{10} cm^{-2} (ref. [29]), and thus drastically longer radiative exciton lifetimes are expected. This is evident in Fig. 4a from the prolonged T_1 lifetime, with the average value of the uncoupled quantum emitters increasing from 4 ns for CVT growth to 13.7 ns for flux growth (Supplementary Note 10). Deterministically coupled quantum emitters in the flux-grown sample display average T_1 lifetimes of 299 ps, corresponding to an average rate enhancement of 48, as well as an average F_P of 185 over the array.

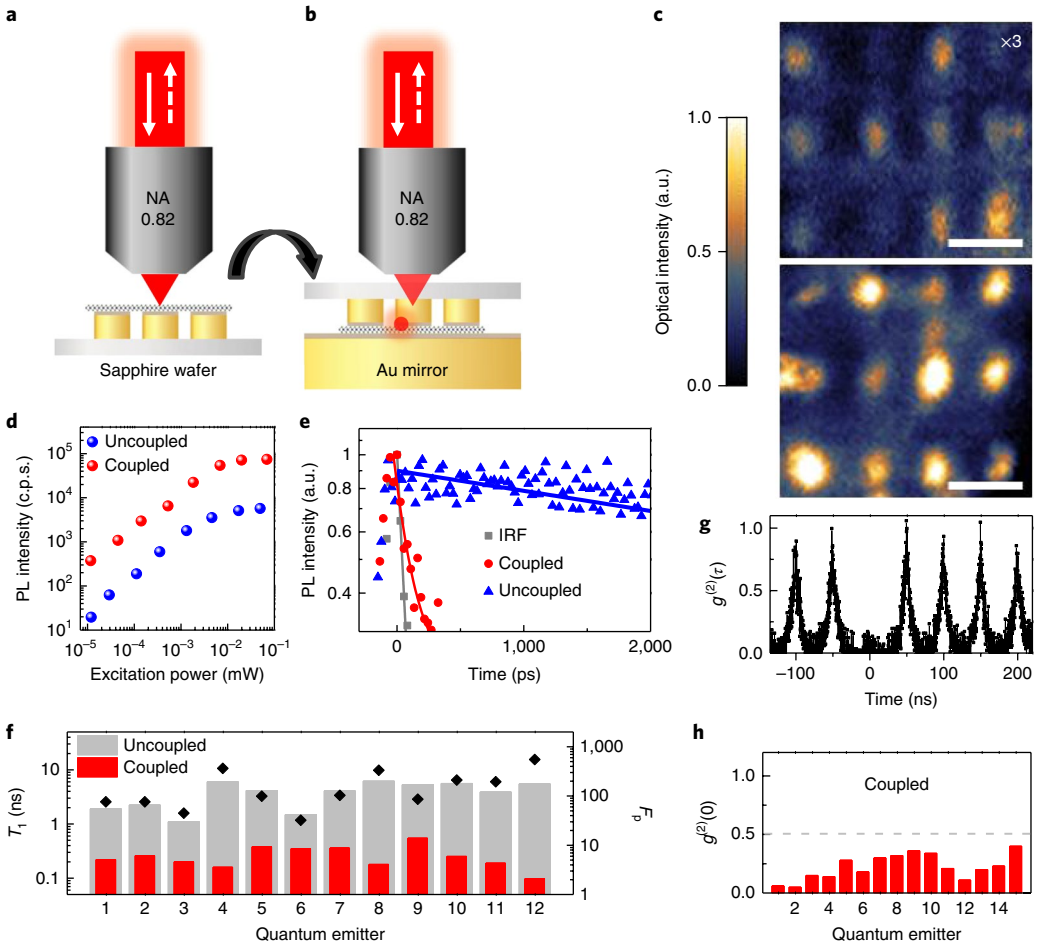

Fig. 3 | Quantifying Purcell enhancement of plasmonically coupled quantum emitters. a,**b**, Schematic of the sample configuration to measure photoluminescence intensity and spontaneous emission rate from each strain-induced quantum emitter before (**a**) and after (**b**) formation of the plasmonic nanocavity by introducing the planar Au mirror. NA, numerical aperture. **c**, Hyperspectral photoluminescence map of a 3 × 4 quantum emitter array recorded through the sapphire side and taken before (top) and after (bottom) the cavity was closed with the planar Au mirror. Note that the scan in the top panel is magnified threefold to illustrate that all 12 sites contain strain-induced quantum emitter emission. Scale bars, 2 μm. **d**, Integrated photoluminescence intensity of an example quantum emitter as a function of excitation power. Blue circles were recorded under the configuration in **a** and red circles for the same emitter location under the configuration in **b**. **e**, Spontaneous emission lifetime (T_1) measurements recorded at 40 μW excitation power. Grey squares show the instrument response function (IRF) for back-reflected laser light. The solid grey line presents the mono-exponential fit representing the system response (65 ps). Blue triangles show results for the isolated quantum emitter without the cavity. The solid blue line is a fit with decay time of $\tau_{off} = 5{,}510 \pm 45$ ps. Red circles show results for the same emitter recorded when coupled to the nanocavity. The solid red line is a fit with $\tau_{on} = 98 \pm 3$ ps. Photoluminescence intensity is shown on a logarithmic scale. **f**, Distribution of T_1 times (left *y* axis) recorded before (uncoupled) and after (coupled) closing the cavity. Diamonds represent the corresponding F_P for each quantum emitter (right *y* axis). **g**, Second-order photon correlation function $g^{(2)}(\tau)$ recorded under pulsed excitation, demonstrating triggered single-photon emission. **h**, Single-photon purity values at zero delay time recorded for 15 coupled quantum emitters on the array.

Importantly, Fig. 4b demonstrates that the flux-grown material already has a high quantum yield of 16.5% in the uncoupled case, which is on a par with the cavity-enhanced quantum yield of CVT-grown material. When coupled, the flux-grown sample displays a record high quantum yield for quantum emitters in 2D semiconductors, with quantum yield values up to 65% (average of 44%, Supplementary Note 7), implying dominant radiative exciton emission in this device. Maximum measured count rates of up to 1.9 MHz (red trace) under pulsed excitation with a 78 MHz repetition rate correspond to triggered single-photon emission rates of 42 MHz into the first lens (Supplementary Note 7). Thus, on average, every second trigger pulse creates a single photon from the device. Figure 4c shows quantum emitter linewidth values recorded at low pump power where pump-induced dephasing is minimized. The corresponding dephasing times reach up to $T_2 = 24$ ps with an average value of $T_2 = 14$ ps (Supplementary Note 11). Given that the T_1 times are Purcell-enhanced under deterministic coupling, this also implies an 88-fold improvement towards reaching the Fourier transform limit ($T_2/2T_1 = 1$), from initially 0.08% ($T_1 = 15{,}000$; $T_2 = 24$ ps) to 7% now ($T_1 = 180$ ps; $T_2 = 24$ ps) in the coupled case and for flux growth.

The demonstrated unity yield for Purcell enhancement of single-photon generation at lithographically defined locations makes the plasmonic nanogap array approach a promising platform for multi-node quantum optical circuits. We note that the cavity-enhanced quantum yield is ultimately limited by the metal loss, and can thus be further improved by reducing the gap size to about $\eta = 80\%$, as was experimentally demonstrated for other quantum emitters[18–20]. Advances in quantum state engineering in 2D materials, for example in forming 2D heterostructures[30] or creating deeper strain

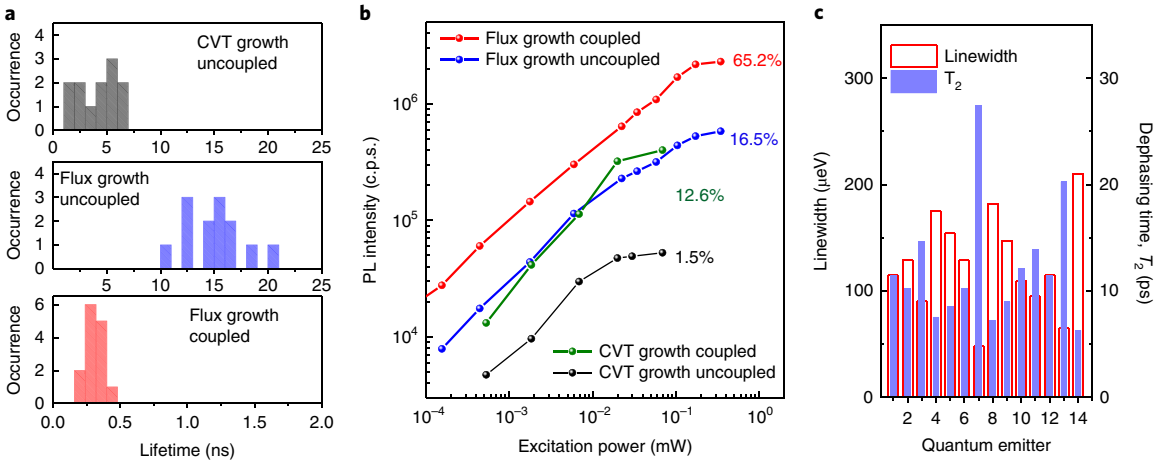

Fig. 4 | Exciton emission lifetime and quantum yield comparing CVT-grown with flux-grown WSe_2. **a**, Occurrence histograms of lifetime values (T_1) recorded while comparing quantum emitters in CVT-grown WSe_2 with quantum emitters in flux-grown WSe_2. **b**, Integrated photoluminescence intensity as a function of excitation power under 78 MHz pulsed excitation, comparing quantum emitters from CVT-grown WSe_2 before (black circles) and after coupling (green circles) with quantum emitters created in flux-grown WSe_2 before and after coupling. Quantum yields determined from pulsed antibunching measurements in the saturation regime are indicated next to each trace. Maximum measured count rates up to 1.9 MHz (red trace) correspond to triggered single-photon emission rates of 42 MHz into the first lens. Thus, on average, every second trigger pulse (78 MHz) creates a single photon (42 MHz) from the device. **c**, Quantum emitter linewidth determined from Voigt deconvolution of the exciton emission spectrum and corresponding dephasing time T_2. All data were recorded at 3.8 K.

potentials, could lead to further improved material quantum yields. The utility of our nanoplasmonic platform can in principle also be extended to other 2D materials such as $MoSe_2$ if deeper strain potentials or cleaner samples that separate sharp emitters better from the ensemble background can be created in future work. The small footprint of the demonstrated 3×4 quantum emitter array and directional outcoupling already allow for efficient butt-coupling to optical fibres. When combined with advances in electroluminescence generation from WSe_2 (refs [31–33]), electrically driven quantum emitter arrays should be within technological reach.

Online content

Any methods, additional references, Nature Research reporting summaries, source data, statements of data availability and associated accession codes are available at https://doi.org/10.1038/s41565-018-0275-z

Received: 18 April 2018; Accepted: 5 September 2018;
Published online: 29 October 2018

References

1. Senellart, P., Solomon, G. & White, A. High-performance semiconductor quantum-dot single-photon sources. *Nat. Nanotech.* **12**, 1026–1039 (2017).
2. Aharonovich, I., Englund, D. & Toth, M. Solid-state single-photon emitters. *Nat. Photon.* **10**, 631–641 (2016).
3. He, Y.-M. et al. Single quantum emitters in monolayer semiconductors. *Nat. Nanotech.* **10**, 497–502 (2015).
4. Chakraborty, C., Kinnischtzke, L., Goodfellow, K. M., Beams, R. & Vamivakas, A. N. Voltage-controlled quantum light from an atomically thin semiconductor. *Nat. Nanotech.* **10**, 507–511 (2015).
5. Koperski, M. et al. Single photon emitters in exfoliated WSe_2 structures. *Nat. Nanotech.* **10**, 503–506 (2015).
6. Srivastava, A. et al. Optically active quantum dots in monolayer WSe_2. *Nat. Nanotech.* **10**, 491–496 (2015).
7. Shepard, G. D. et al. Nanobubble induced formation of quantum emitters in monolayer semiconductors. *2D Mater.* **4**, 021019 (2017).
8. Palacios-Berraquero, C. et al. Large-scale quantum-emitter arrays in atomically thin semiconductors. *Nat. Commun.* **8**, 15093 (2017).
9. Branny, A., Kumar, S., Proux, R. & Gerardot, B. D. Deterministic strain-induced arrays of quantum emitters in a two-dimensional semiconductor. *Nat. Commun.* **8**, 15053 (2017).
10. Strauf, S. & Jahnke, F. Single quantum dot nanolaser. *Laser Photon. Rev.* **5**, 607–633 (2011).
11. Sapienza, L., Davanço, M., Badolato, A. & Srinivasan, K. Nanoscale optical positioning of single quantum dots for bright and pure single-photon emission. *Nat. Commun.* **6**, 7833 (2015).
12. Schnauber, P. et al. Deterministic integration of quantum dots into on-chip multimode interference beamsplitters using in situ electron beam lithography. *Nano Lett.* **18**, 2336–2342 (2018).
13. Riedel, D. et al. Deterministic enhancement of coherent photon generation from a nitrogen-vacancy center in ultrapure diamond. *Phys. Rev. X* **7**, 031040 (2017).
14. Zhang, J. L. et al. Strongly cavity-enhanced spontaneous emission from silicon-vacancy centers in diamond. *Nano Lett.* **18**, 1360–1365 (2018).
15. Schneider, C. et al. Single photon emission from a site-controlled quantum dot–micropillar cavity system. *Appl. Phys. Lett.* **94**, 111111 (2009).
16. Kaganskiy, A. et al. Micropillars with a controlled number of site-controlled quantum dots. *Appl. Phys. Lett.* **112**, 071101 (2018).
17. Akselrod, G. M. et al. Probing the mechanisms of large Purcell enhancement in plasmonic nanoantennas. *Nat. Photon.* **8**, 835–840 (2014).
18. Russell, K. J., Liu, T.-L., Cui, S. & Hu, E. L. Large spontaneous emission enhancement in plasmonic nanocavities. *Nat. Photon.* **6**, 459–462 (2012).
19. Kongsuwan, N. et al. Suppressed quenching and strong-coupling of Purcell-enhanced single-molecule emission in plasmonic nanocavities. *ACS Photon.* **5**, 186–191 (2017).
20. Luo, Y. et al. Purcell-enhanced quantum yield from carbon nanotube excitons coupled to plasmonic nanocavities. *Nat. Commun.* **8**, 1413 (2017).
21. He, X. et al. Carbon nanotubes as emerging quantum-light sources. *Nat. Mater.* **17**, 663–670 (2018).
22. Akselrod, G. M. et al. Leveraging nanocavity harmonics for control of optical processes in 2D semiconductors. *Nano. Lett.* **15**, 3578–3584 (2015).
23. Hoang, T. B., Akselrod, G. M. & Mikkelsen, M. H. Ultrafast room-temperature single photon emission from quantum dots coupled to plasmonic nanocavities. *Nano. Lett.* **16**, 270–275 (2015).
24. Tripathi, L. N. et al. Spontaneous emission enhancement in strain-induced WSe_2 monolayer-based quantum light sources on metallic surfaces. *ACS Photonics* **5**, 1919–1926 (2018).
25. Chikkaraddy, R. et al. Mapping nanoscale hotspots with single-molecule emitters assembled into plasmonic nanocavities using DNA origami. *Nano. Lett.* **18**, 405–411 (2017).
26. Tran, T. T. et al. Deterministic coupling of quantum emitters in 2D materials to plasmonic nanocavity arrays. *Nano. Lett.* **17**, 2634–2639 (2017).
27. Müller, M., Bounouar, S., Jöns, K. D., Glässl, M. & Michler, P. On-demand generation of indistinguishable polarization-entangled photon pairs. *Nat. Photon.* **8**, 224–228 (2014).

28. Zhang, X.-X. et al. Magnetic brightening and control of dark excitons in monolayer WSe_2. *Nat. Nanotech.* **12**, 883–888 (2017).
29. Edelberg, D. et al. Hundredfold enhancement of light emission via defect control in monolayer transition-metal dichalcogenides. Preprint at https://arXiv.org/abs/1805.00127 (2018).
30. Ajayi, O. A. et al. Approaching the intrinsic photoluminescence linewidth in transition metal dichalcogenide monolayers. *2D Mater.* **4**, 031011 (2017).
31. Ross, J. S. et al. Electrically tunable excitonic light-emitting diodes based on monolayer WSe_2 p–n junctions. *Nat. Nanotech.* **9**, 268–272 (2014).
32. Baugher, B. W. H., Churchill, H. O. H., Yang, Y. & Jarillo-Herrero, P. Optoelectronic devices based on electrically tunable p–n diodes in a monolayer dichalcogenide. *Nat. Nanotech.* **9**, 262–267 (2014).
33. Pospischil, A., Furchi, M. M. & Mueller, T. Solar-energy conversion and light emission in an atomic monolayer p–n diode. *Nat. Nanotech.* **9**, 257–261 (2014).

Acknowledgements

The authors thank M. Begliarbekov for supporting the development of the electron-beam lithography process at the City University of New York Advanced Science Research Center (ASRC) nanofabrication facility, and L. Dai for help with designing Fig. 1a. The authors acknowledge financial support to S.S. from the National Science Foundation (NSF) under awards DMR-1506711 and DMR-1809235 and to J.C.H. under awards DMR-1507423 and DMR-1809361. S.S. acknowledges financial support for the attoDRY1100 under NSF award ECCS-MRI-1531237.

Author contributions

S.S. and Y.L. designed the experiment. Y.L fabricated the plasmonic chips. G.D.S. and J.V.A. performed the layer transfer procedures. Y.L. and G.D.S. performed the optical experiments and analysed the data. D.A.R. and B.K. carried out the flux growth. K.B. and J.C.H. supervised the growth. S.S., G.D.S. and Y.L. co-wrote the paper. All authors discussed the results and commented on the manuscript.

Competing interests

The authors declare no competing interests.

Additional information

Supplementary information is available for this paper at https://doi.org/10.1038/s41565-018-0275-z.

Reprints and permissions information is available at www.nature.com/reprints.

Correspondence and requests for materials should be addressed to S.S.

Publisher's note: Springer Nature remains neutral with regard to jurisdictional claims in published maps and institutional affiliations.

Methods

Plasmonic chip fabrication. The Au nanocube arrays were fabricated with an Elionix ELS-G100 electron-beam lithography system using poly(methyl methacrylate) (495 PMMA A4, MicroChem) and developed in methyl isobutyl ketone–isopropanol at a ratio of 1:3 for 180 s. To reduce charging of the non-conductive sapphire substrates during patterning, we introduced either an 8 nm Al layer below the resist or a 10 nm Au layer on top of the resist. To form nanocubes, a 5 nm Ti adhesion layer and a 90 nm Au layer were deposited on the samples with an electron-beam evaporator (AJA Orion 3-TH). The remaining resist was then stripped with warm acetone at 50 °C for 10 min. To create the plasmonic spacer, we used atomic layer deposition to form a 2 nm Al_2O_3 layer on top of the samples. To form the planar Au mirror, a 5 nm Ti adhesion layer and a 100 nm Au layer were deposited by slow-rate electron-beam evaporation onto an epi-ready sapphire substrate with a roughness <0.3 nm, followed by atomic layer deposition of 2 nm Al_2O_3. This approach avoids detrimental trapping of air gaps because of the surface roughness in the planar Au mirror that would otherwise artificially enlarge the plasmonic gap spacing and thus reduce the coupling strength.

Flux growth of WSe_2. The WSe_2 crystals for this study were synthesized by reacting W powder (99.999%) with Se shot (99.999%) at a ratio of 1:20. After loading these materials into a quartz ampoule together with a quartz wool scaffold the ampoule was sealed under a pressure of 1 mtorr and heated to 1,000 °C over a period of 48 h. The temperature was kept steady for 3 days before cooling slowly to 400 °C, followed by centrifugation. Finally, the grown crystals were removed from the scaffold and annealed at 250 °C.

Exfoliation and transfer. Monolayers of WSe_2 were mechanically exfoliated either from commercial crystals (HQ Graphene Company) grown by CVT or from the above-described flux-grown crystals. The plasmonic chips were cleaned in Piranha solution for 5 min and rinsed in deionized water. For layer transfer we followed our previous dry stamping procedure utilizing an elevated substrate temperature of 60 °C to prevent nanobubble formation[7].

Photoluminescence spectroscopy. Photoluminescence measurements were performed at 3.8 K using a closed-cycle cryogen-free cryostat (attoDRY1100, attocube systems AG). For optical excitation we utilized either a laser diode operating at 532 nm in continuous-wave mode, a supercontinuum laser (NKT Photonics) filtered by a 10 nm bandpass centred at 550 nm, or a 405 nm pulsed laser diode (PicoQuant) with variable repetition rate and pulse width of 50 ps. Magnetic fields were applied perpendicular to the plane of the sample within the range 0–9 T. Photoluminescence lifetimes were measured with a supercontinuum laser (78 MHz repetition rate, 7 ps pulse width). Photoluminescence was spectrally filtered around the emission wavelength using bandpass filters and then sent to an optimized avalanche photodiode (IDQuantique) with a low timing jitter of 39 ps. The $g^{(2)}(\tau)$ correlation traces were recorded with a Hanbury Brown and Twiss set-up and analysed with a four-channel time-to-digital converter (HRM-TDC, SensL).

Data availability

The data that support the plots within this paper and other findings of this study are available from the corresponding author upon reasonable request.